




# Analysis and Control of the Gearshift Process Based on a Dog Clutch Shiftability Mode

Ayham Aljawabrah

 <https://orcid.org/0000-0002-7537-6358>

*Department of Railway Vehicles and Vehicle-System Analysis, Faculty of Transportation Engineering and Vehicle Engineering, Budapest University of Technology and Economics,  
Budapest, Hungary  
([aaljawabrah@edu.bme.hu](mailto:aaljawabrah@edu.bme.hu))*

## Abstract

This paper deals with gearshift control using a face dog clutch as a shifting element. Based on our previous work on dog clutch kinematics, the paper identifies optimal control parameters, such as the angular position difference at which the gearshift process can start and the linear reference position trajectory. The robustness of the control parameters is shown. Further on, a gearshift mechanism dynamic model is developed, describing elements of an existing gearbox with shifting elements guided by a rotating disc. The coupled linear and torsional dynamics of the actuated shifting mechanism are analyzed. Finally, a linear quadratic regulator is designed and tested in a model in the loop environment for the requested reference trajectory to show the feasibility of the presented method. Three gearshift cases are considered, and the results show that the developed controller can perform a successful gearshift without experiencing a face impact between the gear and the sliding sleeve teeth in order to enhance sustainability.

## Keywords

Dog Clutch, Control Design, Gearshift, Shiftability, Shifting Mechanism, Simulation

## 1. Introduction

### 1.1. Necessity and classification of gearboxes

Nonrenewable fuel shortages and environmental problems are becoming increasingly pressing global issues, leading the world towards renewable energy sources (Al-Oran et al., 2020) and clean, efficient systems (Burgelman and Grove, 2010). As a result, motor vehicles, including all their subsystems, are receiving more attention for their performance (Alzyod and Ficzero, 2021; Alsardia et al., 2021; Nguyen et al., 2021), efficiency and ability to adopt clean energy concepts (Mallouh et al., 2010, Liu et al., 2021).

Motor vehicles can be cleaner for the environment by optimizing system parameters to be more efficient (Milovančević et al., 2022), specifically the engine and the transmission. Regarding the engine, engine efficiency and alternative fuels can be improved. (Mallouh et al., 2010, Liu et al., 2021, Obeidi et al., 2018)

The development of motor vehicles driven by internal combustion engines (ICE) required the introduction of multi-gear ratio transmissions. The transmission performance depends on several parameters, such as internal structure and operation, power transfer, and gearshift elements.

The operation of a gearbox happens at three levels. The first level is the user interface. At this level, the driver engages in the forward or reverse directions or the neutral position. The driver operates at this level. The second level is the selection of the optimal transmission ratio. The driver can select an algorithm coded in hardware or software. The third level is the mechanical engagement of the selected gear ratio. The driver or an actuated mechanism can also make this level.



From the driver's point of view, vehicle transmission can be classified into two main categories: manual (MT) and automatic (AT). In the manual case, the driver acts at all three levels. In the automatic case, the driver acts only at the first level. Note that in the case of automatic gearboxes, the physical realization and the gear engagement system can be of any convenient type. During the vehicle's operation, the vehicle's selected transmission ratio is influenced by the actual vehicle driving conditions. It is determined by the vehicle's driver in a conventional manual transmission (MT) or by a transmission control unit (TCU) in an automatic transmission. Compared to MT, a TCU chooses more precisely the appropriate gear ratio to operate the ICE in its most efficient torque or power range for a given vehicle load (Rudolph et al., 2007).

Different structures have been developed to provide automatic transmission, such as conventional AT with planetary gearsets, continuously variable transmission (CVT), automated manual transmission (AMT), and dual-clutch transmission (DCT). According to the Council (2015), AT and CVT are better at driving comfort, while MT and AMT are better at efficiency and cost. Regarding driving pleasure, MT and DCT have the edge (Greiner and Grumbach, 2013). In the future, DCTs, ATs, and CVTs are estimated to dominate the passenger car market, while AMTs and MTs will be exclusive in the commercial vehicle market (Xu et al., 2018).

## 1.2. Presentation of the Dog Clutch in the literature

Two traditional solutions exist to fulfil the requirements of easy, silent and smooth gearshift: the synchronizer for manual transmissions and the multi-surface friction clutch for conventional automatic transmissions.. Discussion of the synchronizer and the MSFC supposes that the vehicle's power transmission is partially or completely interrupted at the actual moment, and the research studies phenomena within a short time window (tenths of seconds), before closing the main clutch. Here, we consider the processes at the level of gearbox operation inside the gearbox housing within the duration of the jerk.

The synchronizer has been studied by many researchers (Socin and Walters, 1968; Lovas et al., 2006b; Lovas et al., 2006a). It remained the common gearshift mechanism for many decades, but fuel shortage and environmental issues launched the search for a more efficient system. Initially designed for human operation, the synchronizer employs friction for input-output speed synchronization and stopping mechanisms to empeach gear engagement at high angular velocity difference. Thus, it is not easy to actuate, and it constrains the size of the gearbox.

Dog teeth clutch has been replacing the synchronizer because it provides quicker shifting time, simpler structure, larger power transmitting capacity in identical volume, and has a lower cost (Shiotsu et al., 2019; Vierk and Kowal, 2018), which grants it great potential in several aspects. Heavy-duty electric vehicle (EV) efficiency can be improved by applying multi-speed gearboxes in the transmission chain (Tseng and Yu, 2015). Because of its efficiency, these transmissions employ clutchless automated manual transmission (AMT), using dog clutch as a shifting element. Commercial vehicles equipped with AMT employ the dog clutch as a gearshift element due to its strength and long service life (Bóka et al., 2009).

However, as the mechanical speed synchronization mechanism (the friction mechanism) is missing, the speed synchronization must be a part of the gearshift control. EVs and commercial vehicles utilize an external synchronization strategy for speed synchronization. In the case of EVs employing clutchless AMTs, speed synchronization is achieved by electric motor control (Walker et al., 2017). Commercial vehicles' AMT includes a transmission brake on the gearbox countershaft to set the required low mismatch speed (Bóka et al., 2010a).

In many cases, these strategies cannot be applied. In the case of motorcycles, there is no space to install these components. Also, some conventional ATs utilize the dog clutch as an interlocking element instead of MFSC for fuel efficiency (Dick et al., 2013). In such cases, the gearshift process occurs without speed synchronization, so the shifting process has to be investigated to achieve successful dog clutch engagement.



To the authors' knowledge, these problems were first studied by Laird (1990), who studied the radial and face dog clutch (discussed later) for heavy-duty commercial vehicles. Bóka et al. (2010b) studied the application of the dog clutch shiftability in AMT for commercial vehicles. He used the notion of engagement probability to find a certain successful region depending on the initial mismatch speed and formulated the necessary equations to guarantee successful engagement at a low mismatch speed (below four rad/s).

Later on, Farkas and Lovas (4p, 2014) investigated the engagement process from a kinematical point of view. They developed a geometric condition for successful engagement under constant axial speed and developed a two-dimensional shiftability map. Their results showed a periodicity in the successful shifting region.

In their thesis, Eriksson et al. (2013) conducted a study on the dog clutch used in truck transfer cases, examining the impact of various design parameters, such as geometry and mass, on clutch performance. The study used multibody dynamic simulations and included three different designs with eight sets of parameter combinations. Andersson and Goetz (2010) performed dynamic FEA using Abaqus on the dog clutch to investigate the effect of the chamfer angle, chamfer distance, tooth angle, and axial force. He aimed to find the maximum possible engagement mismatch speed for each tooth geometry and to determine the best one. Duan (2014) developed a dynamic mathematical model for the dog teeth clutch used in automatic transmission for interlocking. The author built a Simulink model and studied the system dynamics response.

Echtler et al. (2017) analyzed the energy-saving potential of a new clutch design called TorqueLINE compared to the conventional one (MFSC) used in automatic transmissions. The study used multibody simulation to analyze different transmission architectures for relevant switching points. The results showed that TorqueLINE significantly reduces drag torques compared to the MFSC. In another paper, Mileti et al. (2019) analyzed the form-fit engagement and performance rating of six dog clutch design variants used in TorqueLINE using SIMPACK multibody simulation. They examined the successful engagement area under various axial and mismatch speeds and found that a dog clutch with a low teeth number, low flank angle, and a high angular gap has the largest successful engagement area. The simulation results were validated with experimental data.

Though the mismatch speed is an essential parameter of the gearshift process of the dog teeth clutch, the dynamics of the integrated gearshift mechanism also have a big influence. Successful dog teeth clutch shifting requires precise pairing between the mismatch speed (angular motion) and the shifting mechanism speed (axial motion). The movement of the shifting mechanism is described by a reference signal tracked by a controller.

Heavy-duty vehicles use pneumatic actuators to perform gearshifts. However, electromechanical gearbox actuators are preferred for heavy-duty EVs, as they allow more precise position control. In (Turner et al., 2007), a direct-drive electromechanical actuation system has been developed for AMT and DCT systems, and a PID controller achieves the position control of the actuator. In (Juhasz et al., 2020), different control algorithms are designed to achieve the position control of an electromechanical shift actuator. Then, the results concerning shift time and real-time applicability are compared. While electromechanical actuators have several advantages, the torsional vibrations and high-speed collisions in the case of failed gear shifts are crucial regarding the expected lifetime of the electromechanical actuator system. Hence, finding accurate shiftability conditions and shifting strategies becomes critical.

In our previous work, we introduced a kinematic model for the dog clutch shiftability and obtained a condition for a successful gearshift, called the shiftability condition, that guarantees an impact-free gearshift process (Aljawabrah and Lovas, 2023b). This work distinguishes between successful and unsuccessful gearshift events, providing a reference signal for a successful gearshift, as will be described in Chapter 3. In another work, we developed a dynamic model for a disk-type cam follower mechanism (Aljawabrah and Lovas, 2022). The used gearbox employs an electromechanical mechanism to control the linear motion of the sliding dog clutch, as will be explained later in Chapter 4. The developed dynamic system is highly nonlinear. Also, in (Aljawabrah and Lovas, 2023a), we developed a dynamic model for the



dog clutch engagement process, dividing the engagement process into four discrete stages and modelling each stage's dynamics. The discrete stages were integrated into one continuous hybrid automata (HA) model to obtain the trajectories of the continuous states. Three gearshift cases are considered to verify the HA model, and Simulink simulation showed that the HA model could capture the continuous states' dynamics inside each discrete stage. These previously mentioned works provide the plant for the system discussed in this paper.

In this paper, we intend to solve a known problem, explained in Chapter 3, for a motorcycle transmission, described in Chapters 2 and 4. This transmission employs dog clutches as gearshifting elements and an electromechanical actuator. The research aims to develop a motion controller that guarantees a face-impact-free (scratching-free) gearshift process. We intend to apply a closed-loop control system that requires a reference signal and a plant where the control action is applied.

The steps of the reasoning are the following:

- Our work on dog clutch kinematics (Aljawabrah and Lovas, 2023b) determines optimal gearshift process parameters at given operating conditions.
- Based on the identified optimal parameters and our work for modelling the shifting mechanism dynamics (Aljawabrah and Lovas, 2022) and the process dynamics for dog clutch engagement (Aljawabrah and Lovas, 2023a), a gearshift algorithm based on the shiftability condition is developed, as well as a controller to control the gear shifting mechanism motion. Simulation results are presented and discussed.

#### Nomenclature

Symbol	Quantity	Symbol	Quantity	Symbol	Quantity
$\xi$	Clutch relative angular position	$\xi_0$	the initial relative angular position	R	electric motor resistance
$\Delta\omega$	mismatch speed	$\phi$	angular pitch	i	electric motor current
$x_0$	axial gap	$x_{fed}$	overlap distance	$K_t$	torque constant
$v_0$	mean linear (axial) velocity	r	the mean radius of the dog clutch	Q	weight on the state error
Z	tooth number	$h_t$	tooth height	$b_{visc}$	viscous friction coefficient
$\phi_t$	angular tooth thickness	$\Phi_b$	angular backlash	$Z_{i,max}$	maximum acceptable error of $i^{th}$ state
$x_s$	linear position of the sliding sleeve	$x_s^*$	linear position reference trajectory	L	electric motor inductance
$\theta$	Disk angular position	t	time	V	input voltage
d	damping coefficient	k	stiffness coefficient	$K_e$	back electromotive force constant
m	mass of the shifting mechanism	J	inertia	R	weight on the input
x	continuous state variables' vector	$F_{act}$	actuator force	K	state-feedback control gain
$T_c$	side (tangential) impact torque	$F_c$	front (axial) impact force	$u_{j,max}$	maximum acceptable value of $j^{th}$ input
<b>Subscripts</b>					
g	meshing gear (input side)	s	sliding sleeve (output side)	k	disk
$s,i$	initial linear position	$s,f$	final linear position	M	electric motor
$s,0$	linear front impact position				

## 2. Presentation of the system

A dog clutch, Figure 1a, is a coupling used to transmit power. It consists of two parts having complementary geometry. These complementary shapes are referred to as dog teeth. The dog teeth can be either on an axial annular



surface (axial dog) or a cylindrical surface (radial dog or spline). The equations describing the teeth engagement are identical for both dog teeth positions. In the following, we consider axial dog teeth only.

The main dog clutch system parameters, shown in Figure 1b and c, are the following: initial relative angular position  $\xi_0$ , mismatch speed  $\Delta\omega_0$ , axial velocity  $v_0$ , axial gap  $x_0$ , overlap distance  $x_{fed}$ , teeth number  $Z$ , and the angular backlash  $\Phi_b$ .

The axial motion of the sliding sleeve realizes the dog clutch engagement. At the beginning of the shifting (Figure 1), the sliding sleeve moves axially with a mean axial velocity of  $v_0$  until the axial gap is crossed (Figure 1e). We suppose a successful engagement happens when an overlap  $x_{fed}$  is reached in the axial direction without face impact (Figure 1f). After the overlap is covered (end of stage 2), several side (tangential) impacts occur between the teeth sides, either at the end of the tangential gap (Figure 1f) or at the start of this gap when the marked black teeth come into contact. The gear will bounce back and forth between these two positions until the mismatch speed is synchronized (equals 0).

Earlier research (Aljawabrah and Lovas, 2023b) has allowed us to develop the shiftability condition described by a double inequality. If the inequality (1) is fulfilled, then the shifting is possible:

$$0 \leq \text{mod} \left( \xi_0 + \Delta\omega_0 \frac{x_0}{v_0}, \frac{2\pi}{z} \right) \leq \Phi_b - \Delta\omega_0 \frac{x_{fed}}{v_0} \tag{1}$$

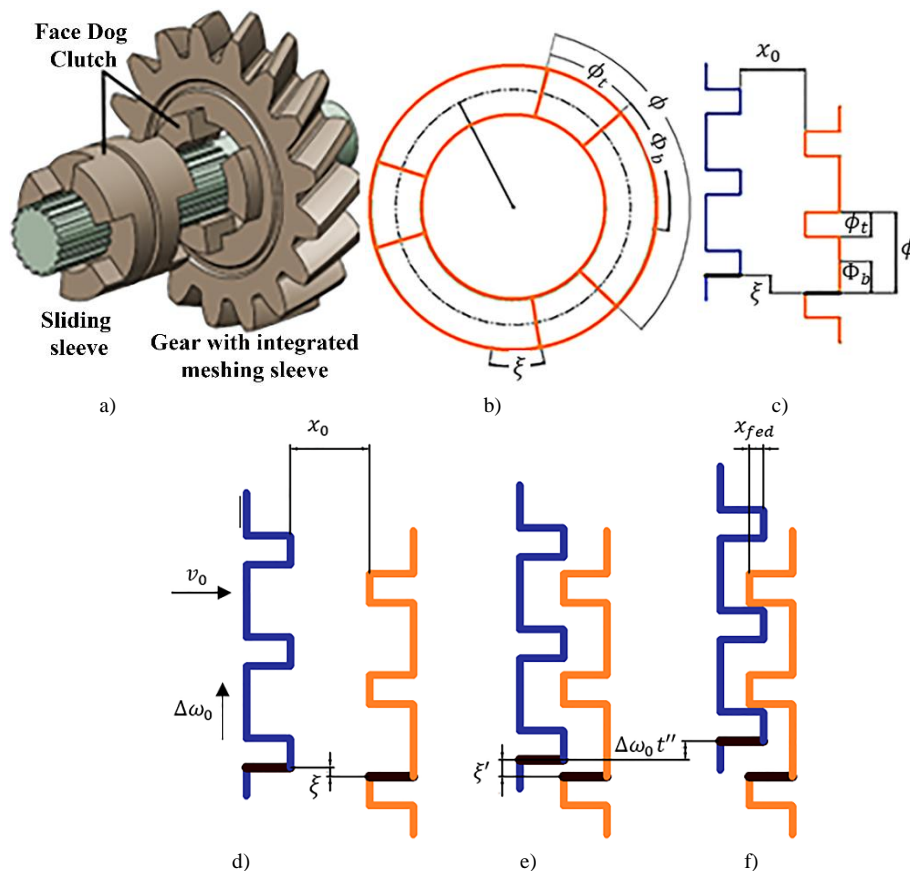


Figure 1. Dog clutch system, a) 3D model and a 2D schematic in a) linear representation, and b) angular representation, d), e), and f) are the engagement stages.

The gearbox that contains the dog clutch is that of an oldtimer motorbike. It has four speeds. This gearbox has the advantage of using both axial and radial dog clutches. Moreover, it has a well-known shifting problem for the 1-2 shift.



This shifting can happen only at small angular velocity differences, as it scratches and does not shift at higher velocity difference values. Further on, the axis of its shifting element, the disk, reaches the outside of the casing, so it is easy to operate it from the outside. Thus, using this gearbox, we can:

- test the fitness of our shifting algorithm,
- test both axial and radial dog teeth
- apply an external actuator easily.

Note that in the case of motorbike gearboxes, it is common to use one common slotted element (disc, cylinder, disc sector) to guide the position of the individual shifting forks.

The shifting mechanism (Figure 2) consists of a shifting motor, a disk-type cam-follower mechanism, and two shifting forks. One fork engages the 1<sup>st</sup> and 2<sup>nd</sup> gears and the other the 3<sup>rd</sup> and 4<sup>th</sup> gears. The linear position of the forks can be at 0 mm (neutral position), 7 mm, or -7 mm as an extreme position where a specific gear will be engaged. A more detailed description of the mechanism and its motion is introduced in Chapter 4.

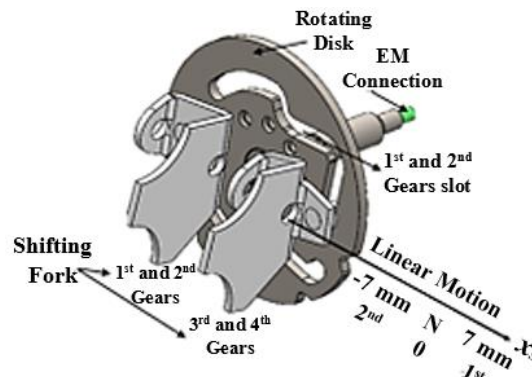


Figure 2. Shifting mechanism 3D model (Aljawabrah and Lovas, 2022)

### 3. Choice of the control parameters

If applying the conditions found above is considered, we must handle the behaviour of the real shifting and actuating parts.

In Eq. (1), the axial speed is considered constant. The axial speed is not constant, as the real actuator force has a non-zero ramp-up duration. Even though the velocity is not constant, Eq. (1) is still valid if the mean axial speed provided by a real actuator and applied to the sliding sleeve is equivalent to the constant speed  $v_0$ . In other words, if an axial velocity  $v_0$  value satisfies the condition in Eq. (1), the actuator should track the reference position  $x_s^*$  subjected to Eq. (2):

$$x_s^*(t) = v_0 t \tag{2}$$

Here, Eq. (2) gives a reference signal with a ramp response. However, a real controller cannot track this perfectly shaped ramp since the system has an acceleration time till reaching the mean linear velocity  $v_0$ . For this reason, the controller shall be robust enough to perform a successful gearshift even though it does not fully track the reference signal. This robustness can be achieved from the dog clutch kinematics.

In (Aljawabrah and Lovas, 2023b), we showed that at a given initial relative position  $\zeta_0$ , and for a linear velocity interval  $(v_{0,min}; v_{0,max})$ , several mean linear velocity values  $v_0$  within this interval could satisfy the shiftability conditions at a given mismatch speed  $\Delta\omega_0$ . The aim is to determine the portion of the predefined interval  $(v_{0,min}; v_{0,max})$  that can satisfy the shiftability condition upon Eq. (1) at a given initial relative position and mismatch speed. To study this, we introduce the notion of probability. The probability shows a successful gear shift's possible for a given mismatch speed



and initial relative position within a predefined mean linear velocity interval ( $v_{0,min}; v_{0,max}$ ). Let's denote the shiftability condition in Eq. (1) by  $G$ . The probability  $P_{vol}(\xi_0, \Delta\omega_0)$  is defined according to Eq. (3):

$$P = \frac{\int_{v_{0,min}}^{v_{0,max}} G(x_0, x_{fed}, z, \Phi_b, \xi, \Delta\omega_0, v_0) dv_0}{v_{0,max} - v_{0,min}} \tag{3}$$

Let us have an example using the parameters of our motorbike gearbox, with its dog clutch parameters, shown in Table 1.

Table 1 Dog clutch parameters

Parameter	Value	Parameter	Value
$x_{fed}$	0.5 mm	$\Phi_b$	34°
$Z$	8	$r$	15 mm
$x_0$ (N-1 <sup>st</sup> )	3 mm	$x_0$ (1 <sup>st</sup> -2 <sup>nd</sup> )	10 mm
$h_t$	4 mm		

Eq. (3) has been plotted in Figure 3a for a mean axial velocity interval of (5; 800) mm/s and the dog clutch parameters, shown in Table 1 that undergo 1<sup>st</sup> to 2<sup>nd</sup> gearshift ( $x_0=10$  mm). Since the results are periodic, the values of  $\xi_0$  have been restricted to be within the interval of (0;  $\phi$ ), here (0; 45°).

Figure 3a shows that at lower  $\xi_0$  values, the maximum probability decreases as the mismatch speed increases. This behaviour is similar to Bóka's model for shiftings at low rpm (Bóka et al., 2010b). Moreover, the maximum probability decreases with the initial mismatch speed. At 50 RPM,  $\xi_0^{max}$  is 42°, and 94% of this interval can guarantee a successful gearshift. Then, at 300 RPM,  $\xi_0^{max}$  is 22°, and the probability drops to 77%. A red dashed line can be drawn using the probability peaks, showing the trend for the optimal initial relative position  $\xi_0^{max}$  for different mismatch speeds.

Figure 3b shows another representation. Here, the  $\xi_0^{max}$  values are shown at different mismatch speeds for two gearshift cases: the neutral to 1<sup>st</sup> gearshift ( $x_0=3$  mm) and the 1<sup>st</sup> to 2<sup>nd</sup> gearshift case ( $x_0=10$  mm). It can be seen that  $\xi_0^{max}$  has a linear relationship with the mismatch speed  $\Delta\omega_0$ . Based on these observations, we can restrict our system so that it performs a gearshift only when the initial relative position  $\xi_0$  is at  $\xi_0^{max}$  at the operating mismatch speed, independently from the moment of the formation of the gearshift order. This assumes the highest shifting probability for the given mismatch speed.

Further, we showed that for a given mismatch speed  $\Delta\omega_0$  and initial relative position, there are split continuous bands of the mean axial velocity within the interval ( $v_{0,min}; v_{0,max}$ ), resulting in a successful gearshift. To illustrate this, the shiftability condition  $G$  (Eq. (1)) has been evaluated at an initial relative position  $\xi_0^{max}=30^\circ$ , and a mismatch speed  $\Delta\omega_0=200$  RPM, at different mean axial velocities  $v_0$  within the interval (5; 800) mm/s. The results in Figure 4a show various split continuous bands where  $G=1$ . For instance, between  $v_0=250$  mm/s and 800 mm/s, a continuous band of mean velocity values can result in a successful gearshift. Also, it shows that the bands are narrow at lower mean velocity values, but their width increases at higher mean velocity. We aim to find the most extended continuous band at the operating mismatch speed.

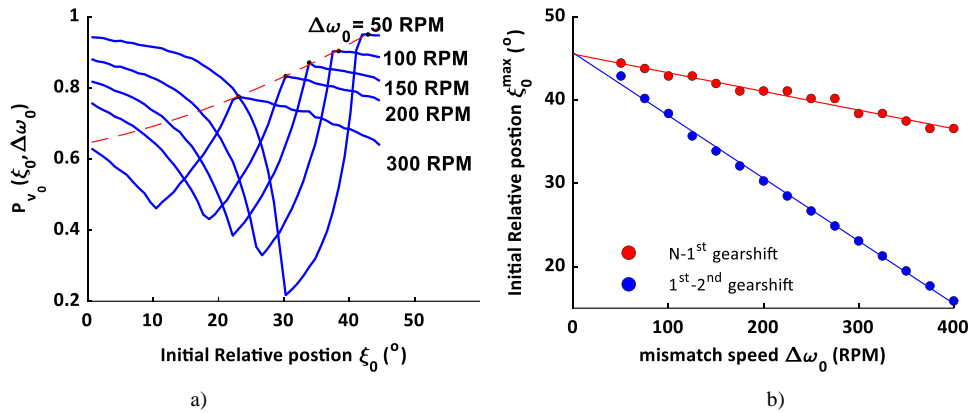


Figure 3. a) Shifting probability variation depending on the initial relative position, and b) Mismatch speed influence on the optimal initial relative position  $\xi_0^{\max}$

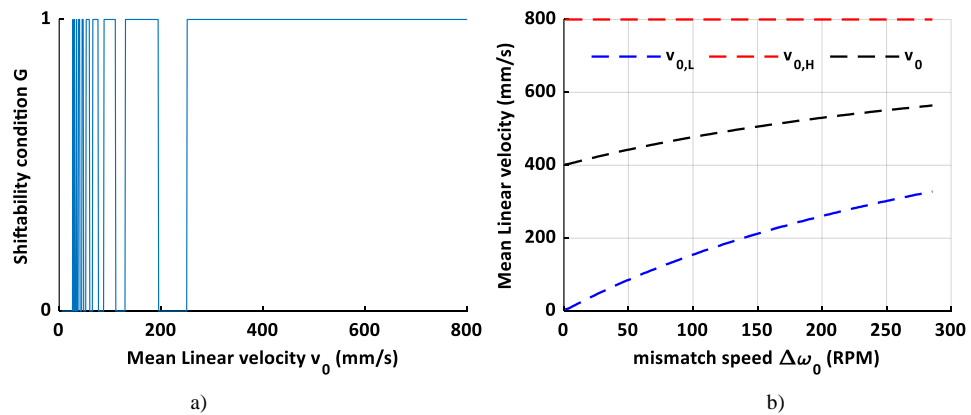


Figure 4. a) Continuous bands for mean linear velocity with  $\xi_{0\max}=30$ , and  $\Delta\omega_0=200$  RPM, and b) Lower and higher mean velocities for the longest continuous band at  $\xi_{0\max}$  in Figure 2b

The existence of these bands grants the controller robustness, and as the band is longer, the controller is more robust. Let us call the velocity at the lower end of the band by  $v_{0,L}$  and the velocity at the higher end by  $v_{0,H}$ . The goal is to find the most extended continuous band with  $G=1$ . This will gain the controller's robustness and improve performance, as illustrated later.

To examine the longest continuous band at different mismatch speeds  $\Delta\omega_0$  with their corresponding  $\xi_0^{\max}$  values, Figure 4b shows the  $v_{0,L}$ ,  $v_{0,H}$ , and their average value  $v_0$ . It shows that the width of the longest band decreases with a higher mismatch speed while  $v_0$  increases.  $v_0$  value is governed by the mismatch speed and the maximal mean velocity  $v_{0,\max}$  of the defined interval  $(v_{0,\min}; v_{0,\max})$ . So, for the same system, a higher  $v_{0,\max}$  can result in a higher  $v_0$ .

Based on these mean velocity values, three different reference positions can be generated according to Eq. (2). These reference positions are  $x_s^*$ ,  $x_s^{*,L}$ , and  $x_s^{*,H}$  generated with  $v_0$ ,  $v_{0,L}$ , and  $v_{0,H}$ , respectively. For instance, from Figure 4b, at a mismatch speed of 150 RPM,  $v_{0,L}$ ,  $v_{0,H}$ , and  $v_0$  are 230, 800, and 515 mm/s, respectively. The obtained  $x_s^*$ ,  $x_s^{*,L}$ , and  $x_s^{*,H}$  reference positions are shown in Figure 5. The controller is imposed to follow  $x_s^*$ . However, it can not follow this function due to the system dynamics since the real system has inertia, and the velocity reaches the prescribed value with a ramp, starting from zero. Meanwhile, if the actual position  $x_s$  lies between  $x_s^{*,L}$ , and  $x_s^{*,H}$  at the impact position  $x_{s,0}$ , which is 3 mm in this case, the controller can successfully perform a gearshift without front impact. In other words, the controller completes the task if:





$$\frac{x_0}{v_{0,H}} \leq t(x_{s,0}) \leq \frac{x_0}{v_{0,L}} \tag{4}$$

The controller is more robust if this time window is wider at the impact position  $x_{s,0}$ .

As the reference trajectory  $x_s^*$  required for the successful shifting has been determined, the next step is to model the shifting mechanism dynamics and develop the controller.

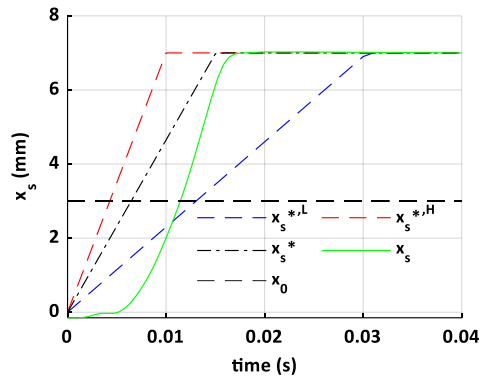


Figure 5. Reference position  $x_s^*$  and real actuator path  $x_s$

However, before introducing the dynamic models, a brief introduction about the gearshift strategy and vehicle velocity path is needed. The vehicle transmission contains several gear ratios, and the gearshift depends on several factors. Usually, the gearshift depends on the road conditions and the drive mode, and there are two strategies for gearshift: fuel economy mode and sport mode. Figure 6 utilizes our considered transmission to show two vehicle speed paths during gear upshift. The gearshift occurs at a lower engine speed in fuel economy mode (path 1). In sport mode, the gearshift occurs at a high engine speed (path 2). Figure 6 shows that the vehicle speed remains constant during the gearshift, but the engine speed steps down due to the gear ratio step. It also shows that the engine speed difference at the gearshift between two successive gear ratios is lower for path 1 than for path 2. The mismatch speed is directly related to the step in engine speed during the gearshift process, and the largest mismatch speed appears between the 1<sup>st</sup> and 2<sup>nd</sup> gearshift. In fact, transmission is considered to have a known problem between the 1<sup>st</sup> and 2<sup>nd</sup> gearshifts, where many face impacts occur, and the sliding sleeve hardly engages due to the high mismatch speed.

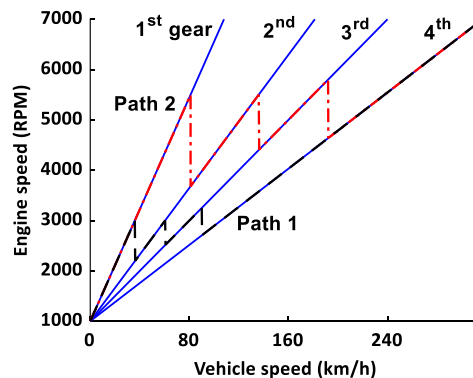


Figure 6. Gearshift and vehicle speed path

This work attempts to solve this problem through an impact-free gearshift, even though a large mismatch speed is present.



The kinematics analysis introduced the shiftability condition (Aljawabrah and Lovas, 2023b), and based on this, the shift mechanism's reference trajectory has been identified. The following chapter intends to complete the path of the dog clutch analysis by looking at the system from a dynamic point of view. In the next two sections, the system dynamics is summarized based on our work in (Aljawabrah and Lovas, 2022) and (Aljawabrah and Lovas, 2023a), and then the controller development is introduced.

#### 4. Dynamics of the shifting mechanism and the dog clutch

As mentioned in the introduction, the transmission has four speeds, employs dog clutches as shifting elements and has an electromechanical gearshift mechanism. The rotational motion of the slotted disk is supplied by a 24 V electric motor directly connected to the disk. This paper focuses on the slot path engaging the 1<sup>st</sup> and 2<sup>nd</sup> gears. It consists of eleven parts: straight lines and circular arcs. At neutral gear, the sliding sleeve is at 0 mm, and then it moves to 7 mm to engage the first gear, and then it moves back to -7 mm to engage the second gear. The produced linear displacement will be a piecewise function of the disk (or electric motor) rotation angle ( $\theta_k$ ). For simplicity, we approximated the piecewise profile by a Fourier series of eight terms, as shown in Eq. (5) (Aljawabrah and Lovas, 2022), and the goodness of the fit is shown in Figure 7.

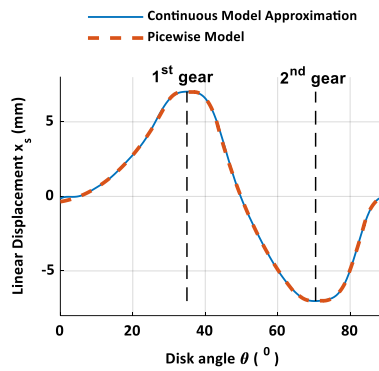


Figure 7. Linear displacement  $x_s$  of the shifting fork depending on the disk angle (Aljawabrah and Lovas, 2022)

Based on our dynamic modeling for the shifting mechanism (Aljawabrah and Lovas, 2022), the shifting mechanism is governed by Eq.(6) and Eq. (7). The electromechanical mechanism's parameters are listed in

Table 2.

$$x_s = a_0 + \sum_1^8 (a_k \cos(k\omega\theta_k) + b_k \sin(k\omega\theta_k)) \quad (5)$$

$$L \frac{di}{dt} + Ri = V - K_e \dot{\theta}_k \quad (6)$$

$$\left( m \left( \frac{dx_s}{d\theta_k} \right)^2 + J_k + J_M \right) \ddot{\theta}_k + m \frac{dx_s}{d\theta_k} \frac{d^2 x_s}{d\theta_k^2} \dot{\theta}_k^2 + F_c \frac{dx_s}{d\theta_k} = K_t i \quad (7)$$

The equivalent inertia is shown in Eq. (8). It is obvious that the system has time-dependent inertia, which is a consequence of the nonlinear relationship between the linear and rotational motion.

$$J_{eq} = m \left( \frac{dx_s}{d\theta_k} \right)^2 + J_k + J_M \quad (8)$$



Table 2 Electromechanical mechanism parameters

Parameter	Value	Parameter	Value
Mechanical part			
m	0.6 kg	J <sub>k</sub>	22.4×10 <sup>-8</sup> kg.m <sup>2</sup>
x <sub>0</sub>	3 mm		
Electric Motor			
R	0.9 Ω	K <sub>t</sub>	0.1125 N.m/A
L	3.2 mH	K <sub>e</sub>	0.191 V.s/rad
J <sub>M</sub>	720×10 <sup>-9</sup> kg.m <sup>2</sup>		

We consider an impact-free gearshift process, so the impact force is set to zero in Eq.(7) during the control design. The system has three states Disk angle  $\theta_k$ , disk speed  $\dot{\theta}_k$ , and motor current  $I$ , and they are referred to as  $x_1, x_2$ , and  $x_3$ , respectively. The system state vector is  $\mathbf{x}$  while its input  $\mathbf{u}$  is the motor voltage  $V$ . Using the Jacobian, the system equations, Eq.(6) and (7), can be linearized at a state vector  $\mathbf{x}_k$ . The state-space matrices are shown in Eq. (9) (Aljawabrah and Lovas, 2022).

$$\begin{aligned}
 \mathbf{A} &= \begin{bmatrix} 0 & 1 & 0 \\ -\frac{A_{211}}{J_{eq}} - \frac{A_{212}}{J_{eq}^2} & \frac{A_{22}}{J_{eq}} & \frac{K_t}{J_{eq}} \\ 0 & -\frac{K_e}{L} & -\frac{R}{L} \end{bmatrix} \\
 \mathbf{B} &= [0 \ 0 \ 1/L]^T \\
 \mathbf{C} &= [1 \ 0 \ 0] \\
 \mathbf{D} &= 0
 \end{aligned} \tag{9}$$

$$\begin{aligned}
 A_{211} &= mx_2^2 \left( \left( \frac{d^2 x_s}{dx_1^2} \right)^2 + \frac{d^3 x_s}{dx_1^3} \frac{dx_s}{dx_1} \right) \\
 A_{212} &= 2m \left( K_t x_3 - mx_2^2 \frac{d^2 x_s}{dx_1^2} \frac{dx_s}{dx_1} \right) \frac{d^2 x_s}{dx_1^2} \frac{dx_s}{dx_1} \\
 A_{22} &= 2 mx_2 \frac{dx_s}{dx_1} \frac{d^2 x_s}{dx_1^2}
 \end{aligned}$$

Now, let us consider the rotational dynamics of the dog clutch inside the gearbox. In (Aljawabrah and Lovas, 2023a), we described a detailed model for the rotational dynamics. We summarize here the important parts related to the control design, considering the face impact-free engagement process. The rotational dynamics model during the free fly phase, stage 1 (Figure 1d), is presented in Eq. (10), and Eq. (11):

$$J_g \ddot{\theta}_g = 0 \tag{10}$$

$$J_s \ddot{\theta}_s = 0 \tag{11}$$

Here, losses are neglected.

At the end of stage 2, when the system reaches the overlap distance (Figure 1f), the sliding sleeve enters stage 3. Several tangential side impacts occur during this stage, resulting in the mismatch speed synchronization. The side impact torque is given in Eq. (12), and the rotational dynamics are shown in Eq. (13)(13) and (14). Here,  $\xi^0$  is the angular position for the side impact.

$$T_c = \begin{cases} k_t(\xi' - \xi'^0) + d_t \Delta\omega & \text{if } \Phi_b \leq \xi'^+ \leq \phi \\ 0 & \text{elsewhere} \end{cases} \tag{12}$$



$$J_s \ddot{\theta}_s = T_c \tag{13}$$

$$J_g \ddot{\theta}_g = -T_c \tag{14}$$

### 5. Control development

Eq. (9) shows that the state-space representation describing the shifting mechanism's behaviour is a Linear Time-Varying (LTV) model. By selecting an appropriate scheduling parameter vector ( $\rho$ ), the system can be modelled using the grid-based Linear Parameter Varying (LPV) framework:

$$\dot{x}(t) = A(\rho(t))x(t) + Bu(t) \tag{15}$$

$$\rho(t) = \left[ x_2(t) \quad x_3(t) \quad \frac{dx_s(t)}{dx_1(t)} \quad \frac{d^2x_s(t)}{dx_1^2(t)} \quad \frac{d^3x_s(t)}{dx_1^3(t)} \right] \tag{16}$$

In the literature, LPV systems are often controlled by high-complexity algorithms such as LPV- $H_\infty$  (Cui et al., 2015) and adaptive MPC (Lee et al., 2017). Such algorithms have exceptional performance but cannot be effectively used in embedded environments due to their high calculation cost. Linear algorithms can also control nonlinear systems by utilizing linearization, gain-scheduling techniques, and cascaded control structures (Prasad et al., 2011). In the presented case, the gear shift is successful if the face dog clutch is reached within the time window defined by the shiftability band. Thus, tracking accuracy is not crucial, and the reference position can be defined freely to a value within the shiftability band. A ramp function is used to generate continuous reference positions to simplify the control design. If the ramp gradient is chosen as the mean of  $v_{0,min}$ , and  $v_{0,max}$ , then the controller's response time can be relatively high, and minor overshoots are also acceptable in the free-fly zone. Thus, there is no need for advanced control techniques, and linear control algorithms can be sufficient. Grid-based LPV models divide the domain of scheduling parameters into a grid and describe the system's behaviour at each grid point using a Linear Time Invariant (LTI) model. Hence, a nominal LTI model must be chosen to use linear control techniques, which can be utilized for controller design.

The reference signal is obtained for the control by checking the dog clutch's relative angular position. The gearshift process can start only if the relative position  $\zeta$  equals  $\zeta_0^{max}$ . At time  $t_0$ ,  $\zeta$  reaches  $\zeta_0^{max}$ , and the controller registers both the current mismatch speed  $\Delta\omega(t_0)$  as initial mismatch speed  $\Delta\omega_0$ , and the initial relative position  $\zeta_0$  as  $\zeta_0^{max}$ .

Since  $\Delta\omega_0 = \Delta\omega(t_0)$ ,  $\zeta_0 = \zeta_0^{max}$ , and the mean linear velocity interval ( $v_{0,min}; v_{0,max}$ ) are known,  $v_{0,L}$ , and  $v_{0,H}$  are determined based on Eq. (1) and  $v_0$  is calculated according to:

$$v_0 = \frac{v_{0,L} + v_{0,H}}{2} \tag{17}$$

We assume a gearshift order arrives at  $0$  s, then  $\zeta$  reaches  $\zeta_0^{max}$  at  $t_0$ . According to this, the reference signal  $x_s^*(t)$  is:

$$x_s^*(t) = \begin{cases} x_{s,i} & t < t_0 \\ x_{s,i} \pm v_0(t - t_0) & t_0 \leq t \leq \frac{x_0}{v_0} + t_0 \\ x_{s,f}^* & t > \frac{x_0}{v_0} + t_0 \end{cases} \tag{18}$$

The generated reference signal is the linear position of the shifting sleeve, but the controller is designed based on the disk angle  $\theta_k$ . So, the current reference linear position  $x_s^*(t)$  is mapped to its corresponding disk angle  $\theta_k^*(t)$  using Eq. (5). The gearshift process is summarized in Figure 8. At time  $0$ s, a gearshift order arrives, and the system registers  $\Delta\omega(0)$  as  $\Delta\omega_0$ , and an array containing the  $\Delta\omega_0$  and  $\zeta_0^{max}$  pairs is stored within the system so that the system can identify  $\zeta_0^{max}$ , given  $\Delta\omega_0$ . The system does request any motion but waits until  $\zeta_0 = \zeta_0^{max}$  and registers  $\zeta_0^{max}$  as  $\zeta_0$ . The mean linear velocity interval ( $v_{0,min}; v_{0,max}$ ) is predefined within the system, and for ease of calculations, this continuous interval is discretized with  $1$  mm/s step, so the continuous interval is converted to a vector with equally spaced elements,  $1$  mm/s step. This vector,  $\Delta\omega_0$ , and  $\zeta_0$  are passed to the shiftability condition in Eq. (1), which results in a vector containing zeros and ones, and its length equals the mean linear velocity vector's length. The system identifies the largest number of



successive elements equal to 1, which is identical to the longest band in Figure 4a. Based on this  $v_{0,L}$ , and  $v_{0,H}$  are determined. Afterward,  $v_0$  is calculated according to Eq. (17), and the system requests a position according to Eq. (18). Here, the role of the controller comes to force the actuator to follow the requested position.

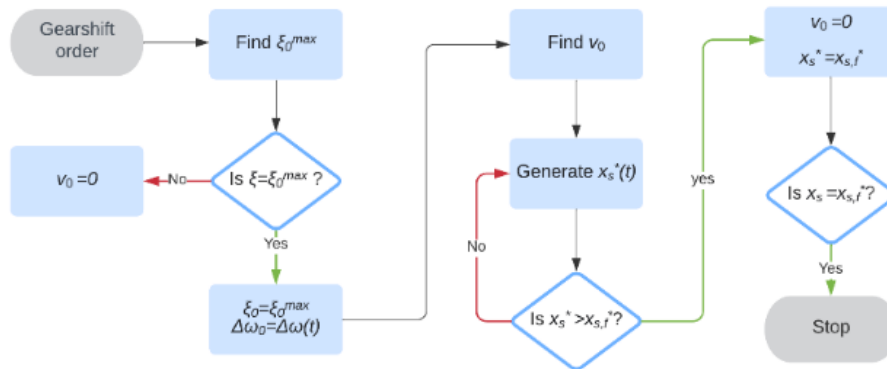


Figure 8. Gearshift process flowchart

By Selecting the nominal LTI model at the  $\rho(t) = \vec{0}$  grid point, the nonlinear elements (e.g., the inertia, load torque) have been omitted or simplified, which leads to the well-known state-space matrix of DC motors:

$$A_{ctrl} = \begin{bmatrix} 0 & 1 & 0 \\ 0 & -\frac{b_{visc}}{J} & \frac{K_t}{J} \\ 0 & -\frac{K_e}{L} & -\frac{R}{L} \end{bmatrix} \quad (19)$$

Using the simplified state-space representation, a Linear Quadratic Regulator has been developed. The LQR control synthesis aims to find a controller, which minimizes the following quadratic cost function:

$$J(u) = \int_0^{\infty} (x^T Q x + u^T R u) dt \quad (20)$$

Then the optimal feedback law, which minimizes the value of the cost, is written as follows:

$$u = -Kx \quad (21)$$

To meet the design requirements and find an appropriate state-feedback controller, the initial weights of the cost function have been chosen using Bryson's rule:

$$Q_{ii} = \frac{1}{z_{i,max}^2} \quad (22)$$

$$R_{ii} = \frac{1}{u_{i,max}^2} \quad (23)$$

Then, they have been finetuned using heuristic methods to achieve the desired performance.

The last step of the controller design is calculating the precompensation gain ( $N$ ). As LQR is a full-state feedback controller, the reference signal must be compensated by considering all the desired steady-state values. The schematic of the closed-loop system is shown in Figure 9.

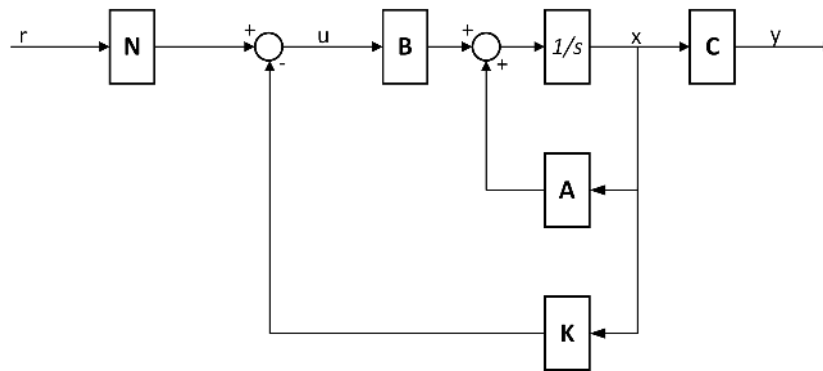


Figure 9. Schematic layout of the closed-loop system

## 6. Simulation results and discussion

### 6.1. Electric motor and shifting disk simulation

The shifting mechanism has been separately simulated on Simulink to study its nonlinear behaviour and shows the system's open-loop response. 5 V constant supply tension was supposed. Several time points in this figure are discussed, and for ease of interpretation, these key time points are named using Latin numbers and shown in the figure. The essential key time points for each subfigure are shown. The same procedure will be used in the following figures.

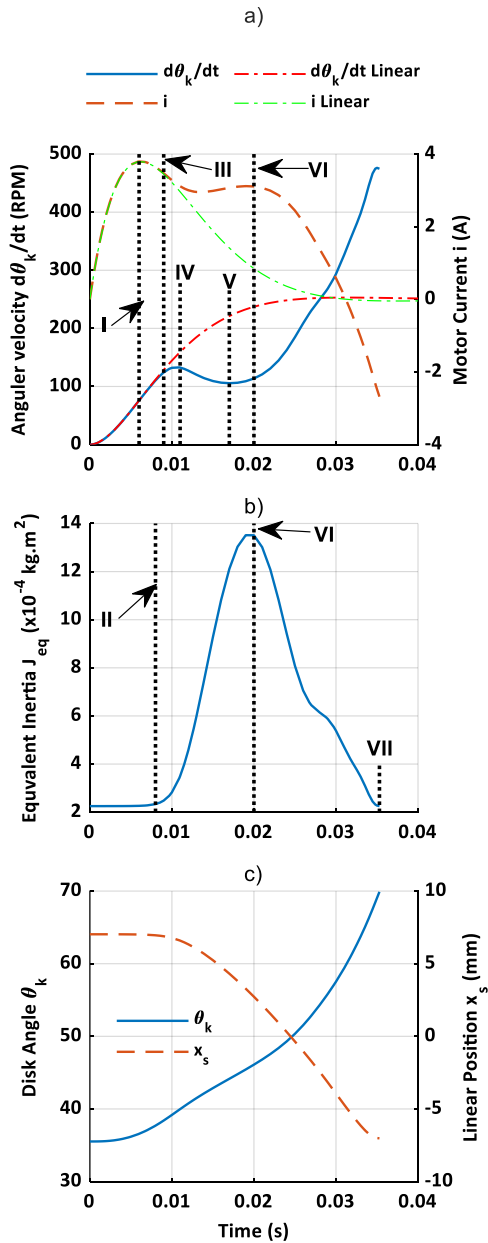


Figure 10 1<sup>st</sup> to 2<sup>nd</sup> gear shift open-loop response without front impact for a) angular speed and motor current, b) equivalent inertia, and c) disk (motor) angle and sliding sleeve linear position. Key time points: I: 0.006s, II: 0.008s, III: 0.009s, IV: 0.011s, V: 0.017s, VI: 0.02s, VII: 0.035s.

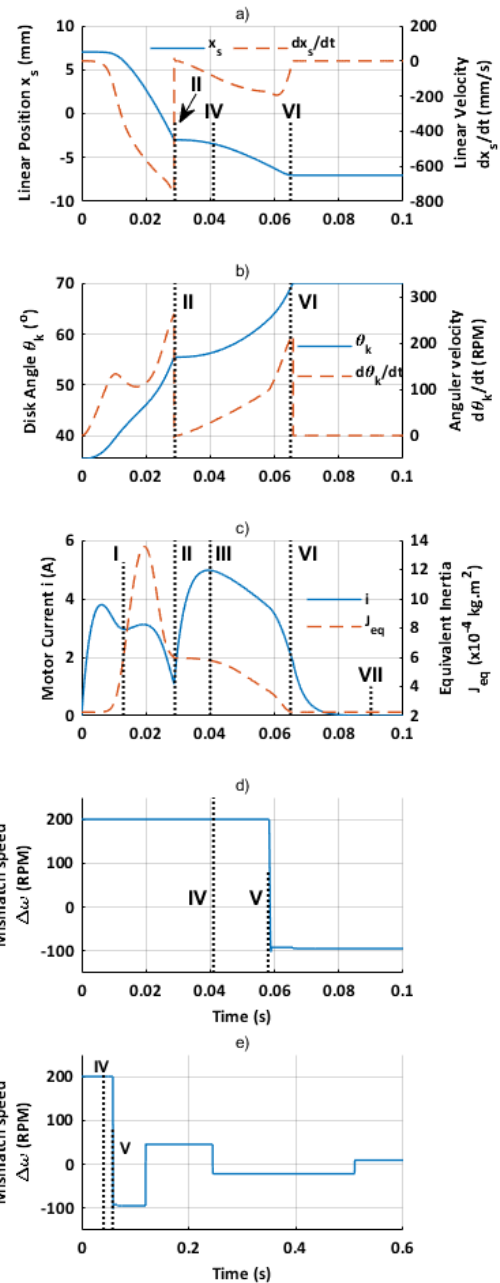


Figure 11. 1<sup>st</sup> to 2<sup>nd</sup> gear shift open-loop response for a) sleeve's linear position and speed, b) disk angle and angular speed, c) motor current and equivalent inertia, and d) Mismatch speed. Key time points: I: 0.013 s, II: 0.029 s, III: 0.04 s, IV: 0.041 s, V: 0.058 s, VI: 0.065 s and VII: 0.09 s.

In Figure 10a, the motor angular velocity increases until time point IV, 0.011 s, and then decreases until time point V, 0.017 s, because of the increased inertia, shown in Figure 10b. The inertia does not change before time point II, 0.008 s, and the motor angular velocity can increase. Then the inertia rises rapidly, and the motor velocity decreases from 0.011 s. Further on, the inertia decreases rapidly from time point VI, 0.02 s, and the motor velocity increases rapidly



from  $0.017\text{ s}$ . Figure 10a shows that the increasing motor velocity decreases motor current from  $0.02\text{ s}$  due to an increasing back electromotive force.

As the inertia does not change before  $0.008\text{ s}$ , Figure 10a shows that the system follows a similar behaviour to a linear system before time point III,  $0.009\text{ s}$ , which can be obtained by setting the mass  $m$  in Eq. (7) to zero. The linear system has a maximum current of  $3.8\text{ A}$  at time point I,  $0.006\text{ s}$  when the motor angular velocity is  $76\text{ RPM}$ . Beyond this time, the motor velocity increases, and the motor current decreases.

The linear system has a steady-state motor velocity of  $250\text{ RPM}$  when the back electromotive force balances the input voltage, while our nonlinear system can reach  $475\text{ RPM}$  (Figure 10a). The system has time-varying inertia, and when the inertia increases, the system stores energy. When the inertia decreases, the stored energy is transferred to the constant inertia part: the motor and disk inertia. This effect is seen in Figure 10a beyond  $0.02\text{ s}$ . From Figure 10b, the system has  $0.0014\text{ kg.m}^2$  inertia at  $0.02\text{ s}$ , but it falls to  $0.0002\text{ kg.m}^2$  at time point VII,  $0.035\text{ s}$ , to one-seventh of the maximum value.

## 6.2. Full system shifting simulation without control.

In what follows, the shifting mechanism model has been integrated with the dog clutch dynamics model. The model shows the system's behaviour in the presence of a front impact force  $F_c$ , under  $5\text{ V}$  constant input voltage. Figure 11 shows the system response for the 1<sup>st</sup> to 2<sup>nd</sup> gearshift with an initial relative position  $\xi_0$  of  $9^\circ$  ( $0.2\phi$ ) and an initial mismatch speed of  $200\text{ RPM}$ .

In Figure 11a, the sliding sleeve starts at  $7\text{ mm}$ , and then freely moves until it hits the gear at  $-3\text{ mm}$ , at the time point II,  $0.029\text{ s}$ . It stops briefly until the next tangential gap passes, then moves until it reaches the final position of  $-7\text{ mm}$ . Before  $0.029\text{ s}$ , the system response in Figure 11 is similar to that in Figure 10 for the corresponding quantities since both cases have no impact.

At time point II,  $0.029\text{ s}$ , and time point I,  $0.013\text{ s}$ , the system has the same inertia value as Figure 11c shows. However, Figure 11b shows that the system has higher angular acceleration at  $0.013\text{ s}$  than at  $0.029\text{ s}$  and a higher current at  $0.013\text{ s}$ , as Figure 11c shows.

When a teeth front impact happens, the linear velocity and the angular velocity fall to zero, as shown in Figure 11a and Figure 11b, but the current increases rapidly due to the absence of the back electromotive force. Figure 11c shows that the current was ramping up towards its theoretical peak value of  $5.6\text{ A}$ , when the shifting mechanism is at rest, but it could reach only  $4.8\text{ A}$  at time point III,  $0.04\text{ s}$ , since the system starts to accelerate; thus, the current decreases. At time point VI,  $0.065\text{ s}$ , the sliding sleeve reaches its final position  $x_{s,f}$ , and the input voltage is set to zero. Note that the current drops to zero at time point VII,  $0.09\text{ s}$ , due to the motor inductance.

From Figure 11a, at  $0.041\text{ s}$ , the sliding sleeve passes to stage 2, which is the end of reaching the overlap at  $-3.5\text{ mm}$ , then the first side impact occurs at time point V,  $0.058\text{ s}$ , as Figure 11d shows. Figure 11e is an extension for Figure 11d with extended simulation time. It shows that several side impacts happen until the mismatch speed is synchronized. The inertia of the output side (the sliding sleeve side) is considered infinite compared to the input side (the meshing gear side). Thus, the angular speed of the meshing gear changes while the angular speed of the dog clutch sleeve is constant. After each side impact, the rotation of the gear is reversed, which is clearly seen in Figure 11e, where the mismatch speed is alternating around zero. The sliding sleeve needed  $0.063\text{ s}$  to reach its final linear position, but it lasted  $0.51\text{ s}$  to synchronize its angular velocity with the meshing gear.

## 6.3. Shifting simulation with LQR control

In the following, an LQR controller has been added to the previously presented system, and the results are shown in Figure 12a-c. The simulation presents a neutral to 1<sup>st</sup> gear shift. The applied initial relative position  $\xi_0$  is  $9^\circ$  while the initial mismatch speed is  $310\text{ RPM}$ . The applied mean velocity interval is  $(5; 800)\text{ mm/s}$ . Figure 12a shows the linear position, while Figure 12b shows the relative angular position  $\zeta$  in the first cycle of one pitch period  $(0, \phi)$  or  $(0; 45^\circ)$ .





At 310 RPM,  $\xi_0^{max}$  is  $38^\circ$ , and a gearshift order arrives at 0 s. Figure 12a shows that the shifting process does not start until the time point I, when the relative position is  $\xi_0^{max}$ , as Figure 12b shows.

At 310 RPM,  $v_{0,L}$ ,  $v_{0,H}$ , and  $v_0$  are 161 mm/s, 800 mm/s, and 481 mm/s, respectively, where they are used to generate the limit reference signals  $x_s^{*L}$ ,  $x_s^{*H}$ , and the reference signal  $x_s^*$  respectively. The sliding sleeve starts at 0 mm, and then moves until it reaches its final position  $x_{s,f}$  at 7 mm. A teeth front impact can occur at a 3 mm, but the controller can successfully closely track the reference signal. The linear position  $x_s$  LQR is between the limit reference signals  $x_s^{*L}$ , and  $x_s^{*H}$  at the impact position  $x_{s,0}$ , so there is no front impact.

In Figure 12b, the relative angular position  $\zeta$  increases from  $9^\circ$  ( $\zeta_0$ ) until it reaches  $45^\circ$  at the time point II, then drops suddenly to zero.  $\zeta$  increases further, but we injected it back to the start of the period ( $0; 45^\circ$ ) to better show the results.  $\zeta$  starts to increase again from  $0^\circ$  until it reaches  $34^\circ$  or  $\Phi_b$  at time point IV, where the first side impact occurs. After the dog clutch passes stage 2, the side impact can happen at two locations within the tangential gap, one at the end of this gap, where  $\zeta$  equals  $\Phi_b$ , or at the start of the gap, where  $\zeta$  equals  $0^\circ$ . The sliding sleeve passed stage 2 at time point III, where  $x_s$  LQR is 3.5 mm, as Figure 12a shows. Figure 12b shows that  $\zeta$  is  $32^\circ$  but the first side impact occurred later at 0.038 s when  $\zeta$  is  $34^\circ$ . After this impact, the gear rotation direction is reversed, and another side impact occurred later at time point V, 0.061 s when  $\zeta$  equals  $0^\circ$ , where the gear rotation direction is reversed again. This causes the relative angular position to be restricted to the backlash interval ( $0; \Phi_b$ ), or ( $0; 34^\circ$ ). Actually, these side impacts continue to occur either at  $0^\circ$  or  $\Phi_b$  relative angular positions until the mismatch speed is synchronized and both the sliding sleeve and the gear move as one unit, where the relative angular position remains at either  $0^\circ$  or  $\Phi_b$ , depending on the last impact location that caused the mismatch speed to be synchronized.

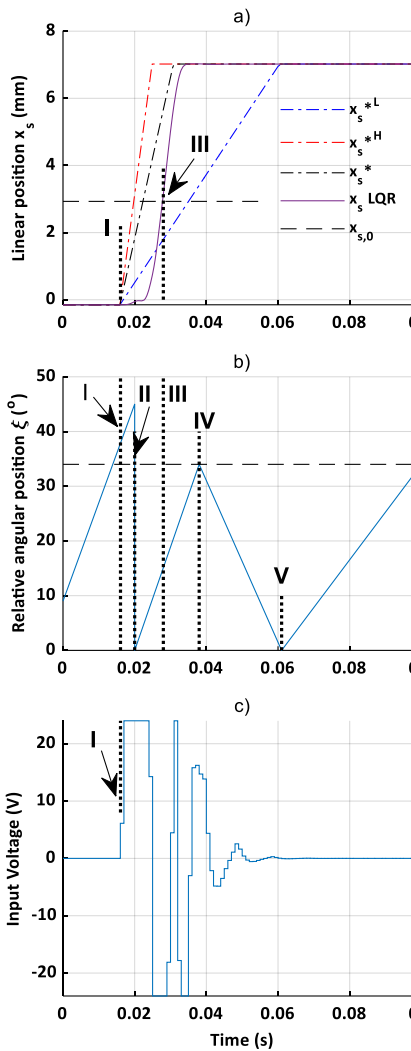


Figure 12. Closed-loop response for N to 1<sup>st</sup> gear. Key time points: I: 0.016 s, II:0.02 s, III:0.028 s, IV:0.038 s, and V:0.061 s.

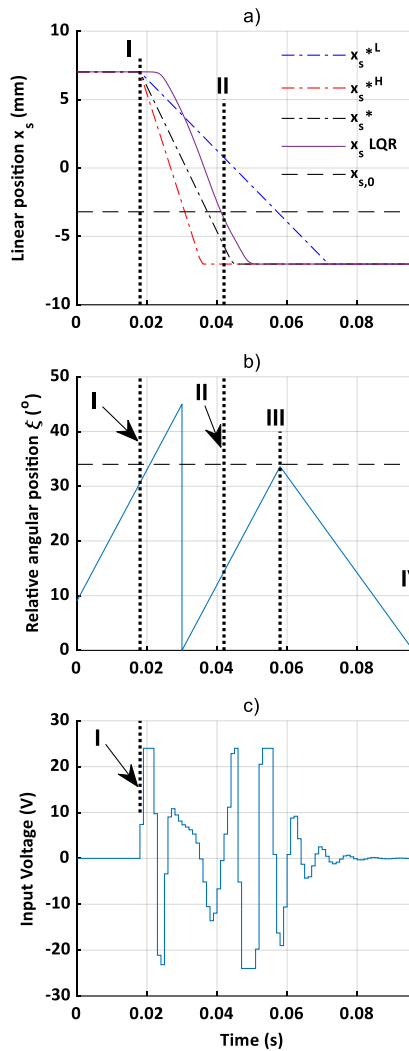


Figure 13. Closed-loop response for 1<sup>st</sup> to 2<sup>nd</sup> gearshift. Key time points: I:0.018 s, II:0.042 s, III:0.058 s, and IV:0.096 s.

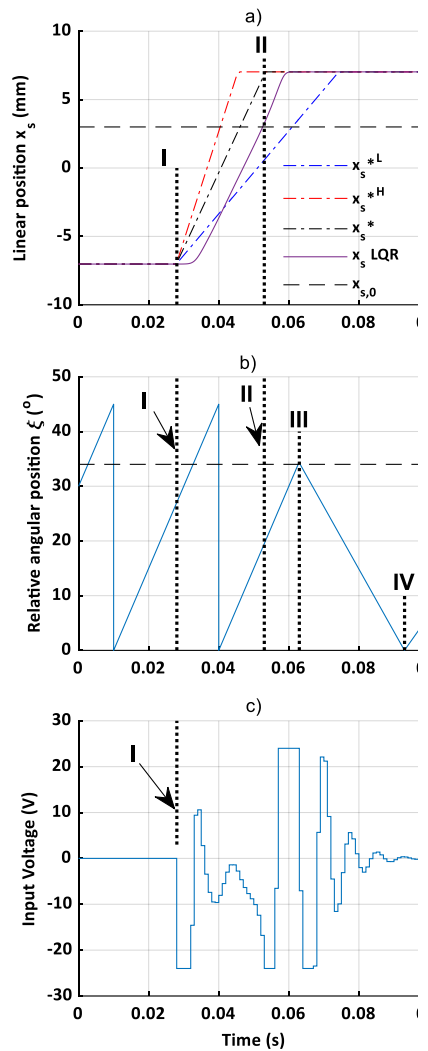


Figure 14. Closed-loop response for 2<sup>nd</sup> to 1<sup>st</sup> gearshift. Key time points: I:0.028 s, II:0.053 s, III:0.063 s, and IV:0.093 s.

A further simulation shows a 1<sup>st</sup> to 2<sup>nd</sup> gearshift. The applied initial relative position  $\xi_0$  is  $9^\circ$ , while the initial mismatch speed is  $200 \text{ RPM}$ . The applied mean velocity interval is  $(5; 800) \text{ mm/s}$ . The LQR controller has been tested; the results are shown in Figure 13a-c. At  $200 \text{ RPM}$ ,  $\xi_0^{\max}$  is  $30^\circ$ , and a gearshift order arrives at  $0 \text{ s}$ . However, Figure 13a shows that the shifting process does not start until time point I, when the relative position is  $\xi_0^{\max}$ , as seen in Figure 13b.

At  $200 \text{ RPM}$ ,  $v_{0,L}$ ,  $v_{0,H}$ , and  $v_0$  are  $261 \text{ mm/s}$ ,  $800 \text{ mm/s}$ , and  $531 \text{ mm/s}$ , respectively, and they are used to generate the limit reference signals  $x_s^{*L}$ ,  $x_s^{*H}$ , and the reference signal  $x_s^*$  respectively. The sliding sleeve starts at  $7 \text{ mm}$ , and then moves until it reaches its final position  $x_{s,f}$  at  $-7 \text{ mm}$ . A teeth front impact might occur at  $-3 \text{ mm}$  linear position, but the controller can perform the gearshift process without impact.

Figure 13b shows that the first side impact occurs at time point III after the sliding sleeve has passed to stage 2. The sliding sleeve passed to stage 2 at time point II, when  $x_s^{\text{LQR}}$  is  $-3.5 \text{ mm}$ , as Figure 13a shows. At this time, Figure 13b shows that  $\xi$  is  $15^\circ$  but the side impact occurs at  $0.058 \text{ s}$ , when  $\xi$  is  $34^\circ$ . Later, another side impact occurs at time point IV, when  $\xi$  is  $0^\circ$ .



Finally, a simulation shows a 2<sup>nd</sup> to 1<sup>st</sup> gearshift. The applied initial relative position  $\xi_0$  is  $30^\circ$  while the initial mismatch speed is  $250 \text{ RPM}$ . The applied mean velocity interval is  $(5; 800) \text{ mm/s}$ . The LQR controller has been tested; the results are shown in Figure 14a-c. At  $250 \text{ RPM}$ ,  $\xi_0^{\max}$  is  $28^\circ$ , and a gearshift order arrives at  $0 \text{ s}$ . However, Figure 14a shows that the shifting process does not start until time point I, when the relative position is  $\xi_0^{\max}$ , as seen in Figure 14b.

At  $250 \text{ RPM}$ ,  $v_{0,L}$ ,  $v_{0,H}$ , and  $v_0$  are  $303 \text{ mm/s}$ ,  $800 \text{ mm/s}$ , and  $552 \text{ mm/s}$ , respectively, and they are used to generate the limit reference signals  $x_s^{*L}$ ,  $x_s^{*H}$ , and the reference signal  $x_s^*$  respectively. The sliding sleeve starts at  $-7 \text{ mm}$ , and then moves until it reaches its final position  $x_{s,f}$  at  $7 \text{ mm}$ . A teeth front impact might occur at a  $3 \text{ mm}$  linear position, but the controller can perform the gearshift process without impact.

Figure 14b shows that after the sliding sleeve has passed stage 2, the first side impact occurs at time point III. The sliding sleeve passed stage 2 at time point II, when  $x_s$  LQR is  $3.5 \text{ mm}$ , as Figure 14a shows. At this time, Figure 14b shows  $\xi$  is  $20^\circ$  but the side impact occurs at  $0.063 \text{ s}$  when  $\xi$  is  $34^\circ$ . Later, another side impact occurs at point IV, when  $\xi$  is  $0^\circ$ .

## 7. Conclusion

Based on the dog clutch kinematics, the optimal relative position  $\xi_0^{\max}$ , which allows the highest successful shifting probability, is determined for different mismatch speeds.  $\xi_0^{\max}$  is the parameter controlling the start of the gearshift process actuation at given operating conditions. The system kinematics study provided that the velocity bands form envelopes that grant the controller robustness.

Further on, the shifting mechanism dynamics have been analyzed. A comparison between the nonlinear and linear model approach showed that the time-varying inertia, which arises from the linearly moving parts and the nonlinear linear-rotational motion relationship, significantly affects the open-loop response for the nonlinear system. The shifting mechanism dynamics were integrated with the dog clutch rotational dynamics to perform a full model simulation and check the open-loop response. The implemented system showed similar results to the shifting mechanism response but only in the zone before an eventual front impact.

The nonlinear dynamics of the shifting mechanism would require a complex controller design, but the existence of the velocity bands (the envelopes) eased the design process. A linearized version of the LPV state-space model could be derived, which led to an LTI state-space system. This LTI system is utilized to design an LQR controller. The controller has been integrated with the complete system model to check its reliability and test our approach of utilizing the velocity bands to generate the reference and limit reference signals. The controller is tested for neutral to 1<sup>st</sup>, 1<sup>st</sup> to 2<sup>nd</sup>, and 2<sup>nd</sup> to 1<sup>st</sup> gearshifts. The results showed that the LQR controller could perform a successful gearshift in both cases without front impact, even though it does not track completely the reference signal.

While this work focused on a specific transmission configuration, it can be extended to other systems using the dog clutch. The models of the kinematics, the dynamics, and the optimal reference trajectory approach remain the same. For a new controller development, the dynamics of a given actuator mechanism have to be integrated with a given dog clutch dynamics to help of development of more sustainable transmission system for vehicles.

A further step in the research will be to test the algorithm with the hardware in the loop, identify the system parameters, and check shiftability in real conditions.

## References

- Al-Oran, O., Lezsovits, F., Aljawabrah, A. (2020): Exergy and energy amelioration for parabolic trough collector using mono and hybrid nanofluids. *Journal of Thermal Analysis and Calorimetry*. 140(3), 1579-1596. DOI: <https://doi.org/ghdrdt>
- Aljawabrah, A., Lovas, L. (2022): Dynamic Modeling of An Electromechanical Gearshift Actuator [in Hungarian: Elektromechanikus Sebességváltó Aktuátor Dinamikai Modellezése]. *Machines* [in Hungarian: GÉP]. 73(3-4), 19-22.



- Aljawabrah, A.Lovas, L. (2023a): Dynamic Modeling of the Dog Clutch Engagement Process Using Hybrid Automata. *Jordan Journal of Mechanical and Industrial Engineering*. 17(1), 127-138. URL: <https://jjmie.hu.edu.jo/vol17/vol17-1/10-JJMIE-278-22.pdf>
- Aljawabrah, A.Lovas, L. (2023b): Kinematical Model of The Dog Clutch Shifting [In Hungarian: Körmös Tengelykapcsoló Kapcsolás Kinematikai Modellje]. *Machines* [in Hungarian: GÉP]. 74(1), 9-12.
- Alsardía, T., Lovas, L.Ficzere, P. (2021) Prototype for fit investigations. *Design Of Machines And Structures: A Publication Of The University Of Miskolc*. 11(1), 5-15.
- Alzyod, H.Ficzere, P. (2021) Potential applications of additive manufacturing technologies in the vehicle industry. *Design Of Machines And Structures: A Publication Of The University Of Miskolc*. 11(2), 5-13.
- Andersson, M.Goetz, K. (2010). FE analysis of a dog clutch for trucks with all-wheel-drive Graduate Thesis. Linnaeus University, Växjö. URL: <https://www.diva-portal.org/smash/record.jsf?pid=diva2%3A634202&dswid=8486>. <https://www.diva-portal.org/smash/record.jsf?pid=diva2%3A634202&dswid=8486> (Downloaded: 20 September 2020)
- Bóka, G., Lovas, L., Márialigeti, J.Trencsényi, B. (2010a) Engagement capability of face-dog clutches on heavy duty automated mechanical transmissions with transmission brake. *Proceedings of the Institution of Mechanical Engineers, Part D: Journal of Automobile Engineering*. 224(9), 1125-1139. DOI: <https://doi.org/bpcw6f>
- Bóka, G., Márialigeti, J., Lovas, L.Trencsényi, B. (2009). External synchronization strategies for automated mechanical transmissions with face dog clutch and countershaft brake. *Proceedings of the 8th International Multidisciplinary Conference*.
- Bóka, G., Márialigeti, J., Lovas, L.Trencsényi, B. (2010b) Face dog clutch engagement at low mismatch speed. *Periodica Polytechnica Transportation Engineering*. 38(1), 29-35. DOI: <https://doi.org/nj85>
- Burgelman, R. A.Grove, A. S. (2010) Toward Electric Cars and Clean Coal: A Comparative Analysis of Strategies and Strategy-Making in the US and China. Research Papers 2048, Stanford University, Graduate School of Business.
- Council, N. R. (2015). Cost, effectiveness, and deployment of fuel economy technologies for light-duty vehicles. National Academies Press, Washington, D.C., USA.
- Cui, L., Chen, L.Duan, D. (2015) Gain-scheduling model predictive control for unmanned airship with LPV system description. *Journal of Systems Engineering and Electronics*. 26(5), 1043-1051. DOI: <https://doi.org/nj86>
- Dick, A., Greiner, J., Locher, A.Jauch, F. (2013) Optimization potential for a state of the art 8-Speed AT. *SAE International Journal of Passenger Vehicle Systems*. 6(2013-01-1272), 899-907. DOI: <https://doi.org/nj87>
- Duan, C. (2014) Analytical study of a dog clutch in automatic transmission application. *SAE International Journal of Passenger Vehicle Systems*. 7(2014-01-1775), 1155-1162. DOI: <https://doi.org/gj3fvb>
- Echtler, P., Mileti, M.Damm, A. (2017) TorqueLine-Konische Kupplung mit Formschluss als alternatives Schaltelement für Automatikkgetriebe. VDI-Fachtagung Kupplungen und Kupplungssysteme in Antrieben, Ettlingen.
- Eriksson, F., Kuttikkal, J. L.Mehari, A. (2013). Parametric study of a dog clutch used in a transfer case for trucks. Graduate Thesis. Linnaeus University, Växjö. URL: <https://www.diva-portal.org/smash/record.jsf?pid=diva2%3A632773&dswid=-8516>. <https://www.diva-portal.org/smash/record.jsf?pid=diva2%3A632773&dswid=-8516> (Downloaded: 22 September 2020)
- Farkas, G.Lovas, L. (2014): Connectivity test of Dog Clutch [in Hungarian: Körmös Tengelykapcsoló Kapcsolhatóságának Vizsgálata]. *Machines* [in Hungarian: GÉP]. LXV.
- Greiner, J.Grumbach, M. (2013) Automatic transmission systems beyond 2020-challenges and competition. *SAE Technical Paper*. 0148-7191.
- Juhász, B., Szabo, A., Becsi, T.Aradi, S. (2020). Control design of an electromechanical gearbox actuator. *Proceedings of the 2020 IEEE 24th International Conference on Intelligent Engineering Systems (INES)*. 109-114.
- Laird, M. P., Lawton, B., and Gregory, R.P. (1990) Dog Clutches for Rapid Gear Changes in Automotive Gearboxes. *Proceedings of the Institution of Mechanical Engineers first international conference*. 102-112.
- Lee, Y., Lee, S.-H.Chung, C. C. (2017) LPV H infinity Control with Disturbance Estimation for Permanent Magnet Synchronous Motors. *IEEE Transactions on Industrial Electronics*. 65(1), 488-497. DOI: <https://doi.org/gfz2f6>
- Liu, D., Li, S.Liu, H. (2021) Experimental Study on Formaldehyde Emission from Environmental Protection and Energy-Saving Alcohol Fuel for Vehicles. *Jordan Journal of Mechanical and Industrial Engineering*. 15(1), 1-6. URL: <https://jjmie.hu.edu.jo/v15-1/01-A81050.pdf>
- Lovas, L., Play, D., Márialigeti, J.Rigal, J.-F. (2006a) Mechanical behaviour simulation for synchromesh mechanism improvements. *Proceedings of the Institution of Mechanical Engineers, Part D: Journal of Automobile Engineering*. 220(7), 919-945. DOI: <https://doi.org/c7tgp3>
- Lovas, L., Play, D., Márialigeti, J.Rigal, J.-F. (2006b) Modelling of gear changing behaviour. *Periodica Polytechnica Transportation Engineering*. 34(1-2), 35-58. URL: <https://pp.bme.hu/tr/article/view/1898>



- Mallouh, M. A., Denman, B., Surgenor, B., Peppley, B. (2010) A study of fuel cell hybrid auto rickshaws using realistic urban drive cycles. *Jordan Journal of Mechanical and Industrial Engineering*. 4(1), 225-229. URL: <https://jjmie.hu.edu.jo/files/v4n1%20wrong%20header/30.pdf>
- Mileti, M., Pointner, L., Pflaum, H., Stahl, K. (2019) TorqueLINE Cone Clutch: Performance Analysis of Highly Dynamic Form-Fit Shifts in Automatic Transmissions. *2019 International Conference on Advanced Vehicle Powertrains*.
- Milovančević, M., Milčić, D., Andjelkovic, B., Vračar, L. (2022) Train Driving Parameters Optimization to Maximize Efficiency and Fuel Consumption. *Acta Polytechnica Hungarica*. 19(3). URL: [https://acta.uni-obuda.hu/Milovancevic\\_Milcic\\_Andjelkovic\\_Vracar\\_121.pdf](https://acta.uni-obuda.hu/Milovancevic_Milcic_Andjelkovic_Vracar_121.pdf)
- Nguyen, D. D., Moghaddam, H., Pirouzfard, V., Fayyazbakhsh, A., Su, C.-H. (2021) Improving the gasoline properties by blending butanol-Al<sub>2</sub>O<sub>3</sub> to optimize the engine performance and reduce air pollution. *Energy*. 218, 119442. DOI: <https://doi.org/gqhf5g>
- Obeidi, T., Larbes, C., Ilinca, A., Filiz, G., Kebir, T. (2018) Fuzzy logic-based maximum power point tracking for a solar electric vehicle. *Acta Polytechnica Hungarica*. 15(7), 133-156. URL: [https://acta.uni-obuda.hu/Obeidi\\_Larbes\\_Ilinca\\_Tchoketch-Kebir\\_86.pdf](https://acta.uni-obuda.hu/Obeidi_Larbes_Ilinca_Tchoketch-Kebir_86.pdf)
- Prasad, L. B., Tyagi, B., Gupta, H. O. (2011). Optimal control of nonlinear inverted pendulum dynamical system with disturbance input using PID controller & LQR. *Proceedings of the 2011 IEEE International Conference on Control System, Computing and Engineering*. 540-545.
- Rudolph, F., Schaefer, M., Damm, A., Metzner, F., Steinberg, I. (2007) The innovative seven speed dual clutch gearbox for Volkswagen's compact cars; Das innovative 7-Gang-Doppelkupplungsgetriebe fuer die Kompaktklasse von Volkswagen.) 28. International Vienna motor symposium.
- Shiotsu, I., Tani, H., Kimura, M., Nozawa, Y., Honda, A., Tabuchi, M., Yoshino, H., Kanzaki, K. (2019) Development of High Efficiency Dog Clutch with One-Way Mechanism for Stepped Automatic Transmissions. *International Journal of Automotive Engineering*. 10(2), 156-161. URL: [https://www.jstage.jst.go.jp/article/jsaeijae/10/2/10\\_20194098/pdf/-char/ja](https://www.jstage.jst.go.jp/article/jsaeijae/10/2/10_20194098/pdf/-char/ja)
- Socin, R. J., Walters, L. K. (1968) Manual transmission synchronizers. *SAE Transactions*. 77, 31-65.
- Tseng, C.-Y., Yu, C.-H. (2015) Advanced shifting control of synchronizer mechanisms for clutchless automatic manual transmission in an electric vehicle. *Mechanism and Machine Theory*. 84, 37-56. URL: <https://doi.org/f6rt3j>
- Turner, A., Ramsay, K., Clark, R., Howe, D. (2007). Direct-drive rotary-linear electromechanical actuation system for control of gearshifts in automated transmissions. *Proceedings of the 2007 IEEE Vehicle Power and Propulsion Conference*. 267-272.
- Vierk, D. T., Kowal, S. J. (2018) Composite friction and dog clutch., US Patent 10,060,485.
- Walker, P. D., Fang, Y., Zhang, N. (2017) Dynamics and control of clutchless automated manual transmissions for electric vehicles. *Journal of Vibration and Acoustics*. 139(6), 061005. DOI: <https://doi.org/gkgmfh>
- Xu, X., Dong, P., Liu, Y., Zhang, H. (2018) Progress in automotive transmission technology. *Automotive Innovation*. 1, 187-210. DOI: <https://doi.org/gp4pww>